Impact of Cascading Faults on Mega-Constellation-Augmented GNSS PPP Integrity

Danielle Racelis, Mathieu Joerger
Virginia Tech, Blacksburg, VA

BIOGRAPHIES

Danielle Racelis obtained a Bachelor's degree in Mechanical Engineering from University of the Philippines in 2014, a second Bachelor's degree in Aerospace Engineering from University of Arizona in 2017, and a Master's degree in Aerospace Engineering from University of Arizona in 2019. She is a PhD student in the Aerospace and Ocean Engineering Department of Virginia Tech, working in the Navigation laboratory for Autonomous Vehicle inTegrity (NAViTi).

Dr. Mathieu Joerger obtained a Master in Mechatronics from the National Institute of Applied Sciences in Strasbourg, France, in 2002. He earned a M.S. in 2002 and a Ph.D. in 2009 in Mechanical and Aerospace Engineering at Illinois Institute of Technology in Chicago. He is the 2009 recipient of the Institute of Navigation (ION) Bradford Parkinson award, and the 2014 recipient of the (ION) Early Achievement Award. He is also an Associate Editor of Navigation for the Institute of Electrical and Electronics Engineers (IEEE) Transactions on Aerospace and Electronic Systems. He is a member of the E.U./U.S. Advanced RAIM (ARAIM) Working Group C. Dr. Joerger is currently assistant professor at Virginia Tech, in Blacksburg, VA, working on multi-sensor integration for safe navigation and collision warning of automated driving systems (ADS).

ABSTRACT

In this paper, we quantify integrity for a GNSS-PPP system when augmented with mega-constellation satellites (GNSS-MC). The geometric diversity provided by signals from fast-moving LEO satellites is exploited for rapid estimation of floating valued cycle ambiguities. Further, the improved redundancy provided by mega-constellation satellite signals in addition to GNSS enable efficient fault detection using carrier phase Advanced Receiver Autonomous Integrity Monitoring (ARAIM). The proposed framework assumes that mega-constellation (MC) satellite orbit and clock determination is based on their spaceborne GNSS receivers. We quantify the impact on integrity of GNSS faults, which not only affect the potential users on earth, but also the spaceborne MC receiver data. Given that GNSS faults can cascade to constellation-wide MC faults, this work determines the conditions where GNSS-MC improves integrity, and quantifies this improvement as compared to GNSS only.

1. INTRODUCTION

With increasing demands on autonomy and navigation safety, quantifying accuracy is insufficient. We need to quantify integrity. So far, the best achievable performance in terms of navigation integrity over wide areas is obtained using carrier phase GNSS positioning and Precise Point Positioning (PPP). For example, one of the most demanding applications motivating the need for GNSS PPP is automated driving systems. GNSS-PPP performance approaches autonomous car navigation integrity requirements [1, 2], but does not quite meet them [3, 4]. In this work, we evaluate the integrity performance of GNSS-PPP augmented with low earth orbit (LEO) satellites.

In carrier phase GNSS, changes in satellite geometry can be exploited to provide quick and accurate estimation of floating-point cycle ambiguities [5, 6]. But, the large amount of time for GNSS spacecraft to achieve significant changes in line of sight results in long initialization times, and limits the use of carrier phase GNSS in most real-time applications. The geometric diversity needed for prompt carrier phase positioning can potentially be provided by emerging LEO satellite constellations launched by private companies such as SpaceX and Amazon. In contrast to GNSS at medium earth orbit (MEO), angular variations from LEO satellites quickly become substantial. SpaceX's plans to deploy tens of thousands of satellites in LEO could also result in a significant increase in redundant ranging measurements. Therefore, the combination of LEO mega-constellation and GNSS observations can make timely, global, robust, and unambiguous carrier phase positioning possible.

The use of LEO satellites for improved navigation performance is not unexplored. The underlying concept of using satellite motion to resolve carrier phase cycle ambiguities is equivalent to the principle of Doppler positioning used in Transit, the first operational satellite

 https://doi.org/10.33012/2020.17669

radio-navigation system. Using Transit's constellation of LEO satellites, the position of stationary receivers could be determined with better than 70 meters of accuracy [7]. The most compelling proof of concept for LEO-based carrier phase positioning without the stationary user restriction was realized in the late 1990's by Rabinowitz et al. [8], with the development of a receiver capable of tracking carrier phase measurements from GPS and from GlobalStar (another LEO telecommunications constellation). In [9], the augmentation of GPS with LEO Iridium satellite signals provided signal redundancy, and enabled fault detection using carrier phase ARAIM. Another implementation can be found in [10] where LEO satellite signals were used to limit the drift of inertial sensors in GPS-denied areas. Reference [11] assessed the performance achieved by augmenting GNSS with measurements from a lone LEO satellite (Luojia-1A) carrying a navigation payload capable of automatically calculating its orbit and clock by itself. Recent work in [12, 13, 14] examined several aspects that could allow LEO mega-constellations to act as navigation satellites.

Apart from Iridium-GPS, there has not been much analysis on the integrity of LEO-augmented GNSS systems. In response, this research focuses on safety-critical navigation applications where integrity is of primary concern. Integrity risk is the probability of undetected faults causing unacceptably large positioning errors. Can mega-constellations, when combined with GNSS and PPP corrections, contribute to achieving safety-critical integrity risk requirements?

In prior work [15], we evaluated the integrity performance achieved by a notional mega-constellation-augmented GNSS (GNSS-MC) architecture assuming fault-free conditions, and concluded that GNSS-MC has the potential to reduce the achievable horizontal alert limit. Since the mega-constellations are primarily intended for communication, assumptions were made regarding the space, ground, and user segments that would allow these LEO constellations to be used for navigation. An estimation algorithm was derived for integrating dual-frequency measurements from GPS and Galileo, with dual-frequency carrier phase measurements from OneWeb and Boeing mega-constellations, which leveraged satellite motion to determine floating-valued cycle ambiguities. We designed a batch estimator to account for time correlation in the errors through newly derived measurement error models that still need to be validated.

In this paper, we modify and extend the prior analysis to incorporate signal-in-space fault hypotheses, e.g., including excessive spacecraft clock drift. We develop a fault detector and evaluate the impact of undetected satellite faults on integrity risk. In risk evaluation, we want risk estimates to upper-bound the actual risk. For lack of knowledge on rarely-occurring fault magnitude distributions, we need to account for the *worst case* fault model over time, which maximizes the predicted integrity risk. In parallel, we can use robust, over-bounding probabilistic models [16, 17] for satellite orbit and clock errors, tropospheric delays, and multipath and receiver noise. While *snapshot* error models for GNSS are well established [18], error models *over time* for GNSS and for LEO are not as well understood. In response, in this work, we refine the time-correlated measurement error models by using a sequential estimation error bounding method developed in [19, 20], with high-integrity models developed in [21, 22], to conservatively account for time correlation in satellite orbit and clock ephemeris errors, tropospheric delay, and multipath.

Section 2 of the paper describes an assumed system architecture for the combined constellation where MC orbit and clock determination (OCD) is performed using MC-embedded GNSS receivers. Starlink mega-constellation satellites are used as examples, but the methods presented in the paper can be adapted to other LEO constellations if their spacecraft have similar capabilities (including spaceborne GNSS receivers). The third section describes the estimation and fault detection algorithms. Based on the system architecture described in the first section, MC orbit and clock determination using spaceborne GNSS receiver data is not only impacted by MC satellite clock faults, but also by GNSS-based MC orbit determination faults. This research explores this *cascading fault* effect of using GNSS-derived MC positions. In the last section, we evaluate the integrity performance of the combined constellation. This research provides methods to analyze the potential of mega-constellation-augmented GNSS to achieve safety critical navigation requirements in air and land transportation applications.

2. GNSS-MC SYSTEM ARCHITECTURE

In order to evaluate the potential performance of a GNSS-MC system, we make assumptions on the space, ground, and user segment that will allow such a navigation system to function. The performance evaluation will be based on assumed characteristics of the example MC satellite signals including their frequency and footprint. We assume the user has access to PPP corrections, and this is reflected in the measurement error parameter values in Section 3.

2.1. Envisioned GNSS-MC System Overview

Constellations. We use GPS and Galileo for GNSS. We quantify the expected integrity performance of an assumed MC configuration, modeled after Starlink as an example. In this work, we consider 27-satellite GPS, 27-satellite Galileo, and 1584-satellite MC. The simulated MC shown in Fig. 1 is based on the first shell in Phase 1 of Starlink constellation deployment [23].

Ranging. For ranging measurements, we assume that the ground user can get dual frequency code and carrier measurements from GNSS, and dual-frequency carrier phase measurements only from MC satellites. The measurements from MC satellites are assumed to be carrier-phase-based so that ranging to the satellite can be incorporated with data sent during downlink communication. The LEO transmitter antenna beam is designed to ensure continuous Earth surface coverage while limiting overlap between satellites in adjacent orbital planes [24]. According to SpaceX's FCC filings [23], ground users can receive Starlink signals at a minimum elevation angle of 25° in the early phases of constellation deployment, and 40° once the full constellation is deployed. In our simulations, we assume a ground user elevation mask of 5° for GNSS, and 40° for MC. It is clear in Figure 2 that relative to a user on the ground, GNSS satellites barely move, while MC satellites passes are substantial. We leverage MC satellite motion to enable quick and unambiguous carrier-phase positioning. However, this satellite motion is limited to MC signals received at angles above the elevation mask of 40°.

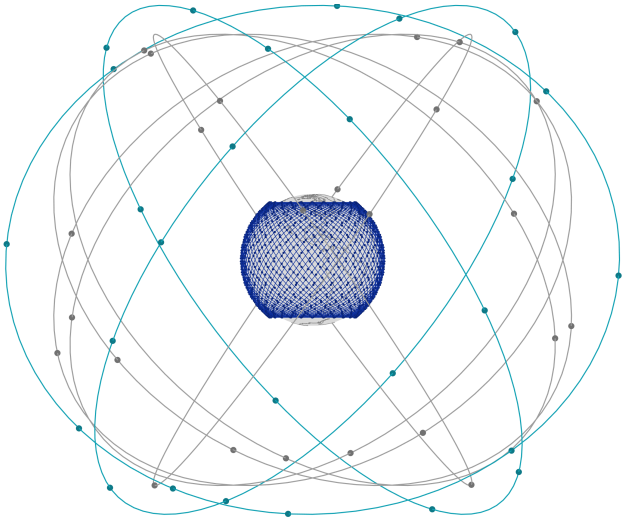

Figure 1: GNSS-MC. The simulation uses 27-satellite GPS (shown in gray), and 27-satellite Galileo (shown in teal). The 1584-satellite Starlink constellation (shown in blue) used in the simulations has 72 orbital planes inclined at 53° at 550 km altitude [25, 24].

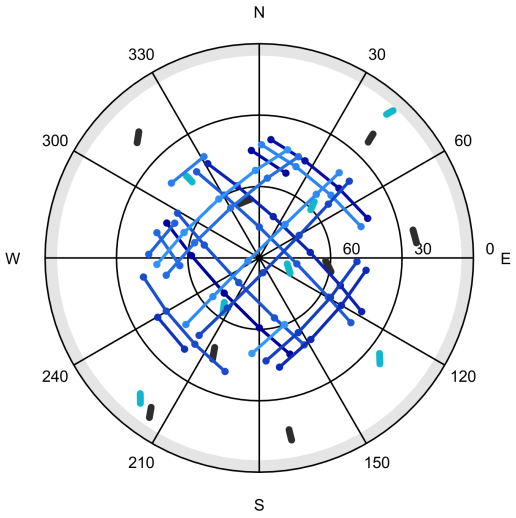

Figure 2: Azimuth-Elevation Plot. This azimuth-elevation plot shows a sky view of the satellite positions over 10 minutes for GPS in gray, Galileo in teal, and MC in shades of blue. The dots indicate the satellite positions at 30-second intervals.

MC Orbit and Clock Determination (OCD) We assume the MC satellites carry a hosted payload consisting of a dual-frequency GNSS receiver and antenna. The spaceborne receiver gives the MC satellite its position, velocity and clock offset. In addition to ranging measurements, MC satellites send their GNSS-derived pose to a dedicated network of ground stations, which computes and disseminates the MC orbit parameters to the users. With this framework where MC satellites derive their pose using GNSS satellites, using mega-constellation signals not only introduces more fault sources, but in addition may also be impacted by GNSS faults. Given that GNSS faults can cascade to constellation-wide MC faults, a key objective of this work is to determine the conditions where GNSS-MC improves integrity, and quantify this improvement.

2.2. GNSS-MC Assumed Architecture

To determine whether or not it is even worth considering MC-augmentation, we put together a GNSS-MC framework based on the existing GNSS-PPP architecture. This framework is illustrated in Figure 3. The basis for the GNSS-PPP system is shown with gray text, boxes, and arrows. The ground user is equipped with a PPP-enabled GNSS receiver with ARAIM. There is a dedicated network of PPP reference stations which tracks the GNSS satellites, calculates precise GNSS ephemeris and integrity parameters, and provides alerts and GNSS corrections to the ground user through cellular signals, and through PPP-dedicated geostationary satellites.

The proposed MC-augmentation is shown with black text, boxes, and arrows in Figure 3. We assume that the ground user can measure range to MC satellites using carrier-phase measurements. The MC satellites are equipped with GNSS receivers and integrity monitoring for real-time navigation, onboard time-synchronization, and GNSS fault detection. MC satellites provide ranging measurements and its GNSS-derived pose, with some guaranteed GNSS fault detection probability to the reference stations. There, it is processed to produce precise MC ephemeris that is sent to the users through the PPP network. The network of reference stations is assumed to provide precise MC orbit and clock ephemeris with integrity monitoring.

It is important to keep in mind that this is an example framework. We define the framework with and without MC to allow quantification of the relative performance between using GNSS-PPP, and using GNSS-PPP-MC. For now, we are not accounting for the correlation between MC positioning errors and user positioning errors, which are both using GNSS measurements. Part of what mitigates that correlation is the fact that the MC OCD process (gathering data, computing orbit ephemeris, and disseminating information to users) takes time. Thus, it is likely that the MC orbit and clock errors impacting the ground user depends on past-time GNSS measurement errors and is dominated by prediction errors.

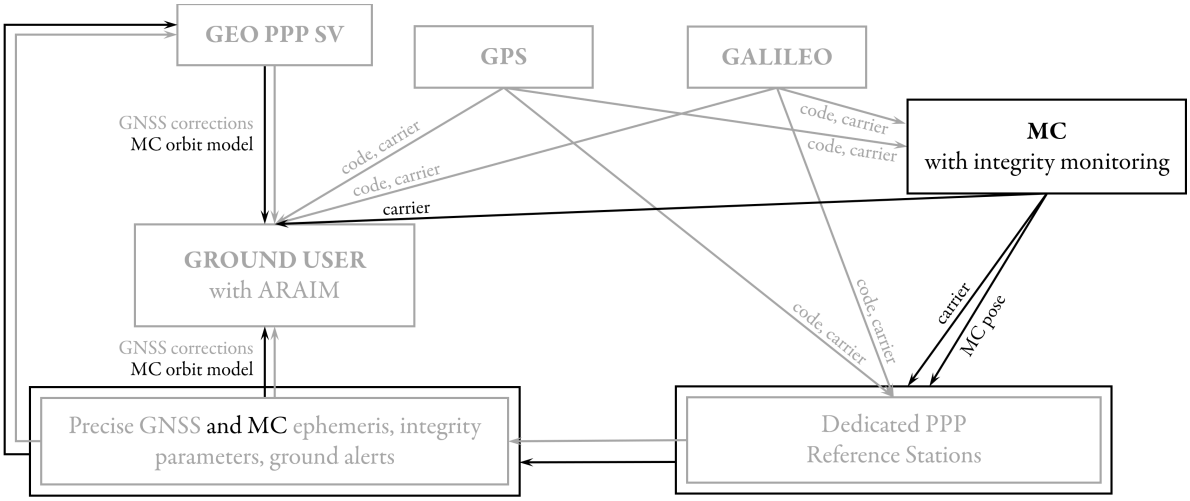

Figure 3: Overview of a GNSS-PPP Architecture Augmented with MC. The basis for the GNSS-PPP system is shown in gray, and components for MC-augmentation is shown in black.

3. NOMINAL MEASUREMENT ERROR MODELS ACCOUNTING FOR TIME-CORRELATION

Assumptions were made in [26] to justify error models for LEO single-frequency ranging measurements. However, signals from fast-moving LEO satellites cross wide sections of the atmosphere within a few minutes, which makes modeling of ranging errors due to the atmosphere extremely challenging. Moreover, addressing ionospheric anomalies in safety-critical applications is exacting [27, 28]. In response, in this preliminary analysis, we assume dual-frequency carrier measurements from MC satellites (no code), which are used to eliminate the impact of ionospheric errors. Models for the remaining errors including satellite orbit and clock ephemeris, tropospheric delay, multipath, and receiver noise are discussed next.

We assume that the ground user receives frequent PPP updates. The errors are modelled as in [15] with refinements to account for PPP corrections. The linearized ionosphere-error-free carrier phase and code measurement equations for satellite i at time k respectively are

$$\begin{aligned} {}^{i}\phi_k &= -{}^{i}\mathbf{e}_k^{\mathrm{T}}\mathbf{x}_k + \tau_k + {}^{i}\eta + {}^{i}\mathcal{E}_{E,k} + {}^{i}\mathcal{E}_{T,k} + {}^{i}\mathcal{E}_{M,\phi,k} + {}^{i}\mathcal{E}_{R,\phi,k} \\ {}^{i}\rho_k &= -{}^{i}\mathbf{e}_k^{\mathrm{T}}\mathbf{x}_k + \tau_k \qquad + {}^{i}\mathcal{E}_{E,k} + {}^{i}\mathcal{E}_{T,k} + {}^{i}\mathcal{E}_{M,\rho,k} + {}^{i}\mathcal{E}_{R,\rho,k} \end{aligned} \tag{1}$$

where ${}^{i}\phi_k$ is the carrier phase measurement, ${}^{i}\rho_k$ is the code phase measurement, ${}^{i}\mathbf{e}_k$ is the 3×1 line-of-sight vector from the satellite to the user in North-East-Down (NED), $\mathbf{x}_k$ is the user position with respect to the linearization point, τ_k is the receiver clock offset (one for each constellation), ${}^{i}\eta$ is the carrier phase cycle ambiguity (there is no subscript k because it is constant over time), ${}^{i}\mathcal{E}_{E,k}$ is the satellite orbit and clock ephemeris error, ${}^{i}\mathcal{E}_{T,k}$ is the residual tropospheric error, ${}^{i}\mathcal{E}_{M,k}$ is the multipath error, and ${}^{i}\mathcal{E}_{R,k}$ is the receiver noise error.

3.1. Satellite Orbit and Clock Ephemeris Error

The error due to satellite orbit and clock for satellite i at time k is modelled as a first-order Gauss-Markov Process (FOGMP)

$${}^{i}\mathcal{E}_{E,k} = e^{-T_s/T_E}\,{}^{i}\mathcal{E}_{E,k-1} + \nu_{E,k} \qquad , \qquad \nu_{E,k} \sim N\left(0, \sigma_E^2\left(1 - e^{-2T_s/T_E}\right)\right) \tag{2}$$

where T_E is the Markov process correlation time constant, $\nu_{E,k}$ is the driving noise, $T_s = t_k - t_{k-1}$ is the sampling interval, and σ_E is the GMP standard deviation. We assume no correlation between measurements from different satellites [29, 30, 31]. The GMP

standard deviation and correlation time constant for ground vehicle applications are given in Table 1 for GNSS [4, 21, 32]. The GMP standard deviation for MC ephemeris is assumed to match GNSS.

3.2. Residual Tropospheric Error

The bulk of the tropospheric delay error is removed using standard models of the troposphere [33]. We model the residual tropospheric error as a FOGMP scaled by an elevation-dependent tropospheric correction mapping function [34]

$$ {}^{i}c_{T,k} = \frac{1.001}{\sqrt{0.002001 + (\sin({}^{i}\theta_{k}[\text{rad}]))^{2}}} \tag{3} $$

for satellite elevation angles ${}^{i}\theta_{k} \geq 4^{\circ}$. The resulting error contribution for satellite i at time k is given by

$$ {}^{i}\mathcal{E}_{T,k} = {}^{i}c_{T,k}\, {}^{i}\zeta_{T,k} \,. \tag{4} $$

The residual tropospheric error at zenith is modeled as

$$ {}^{i}\zeta_{T,k} = e^{-T_s/T_T}\, {}^{i}\zeta_{T,k-1} + \nu_{T,k} \qquad , \qquad \nu_{T,k} \sim N\left(0, \sigma_T^2 \left(1 - e^{-2T_s/T_T}\right)\right) . \tag{5} $$

The GMP parameters are given in Table 1, where $(0.05\text{ m})^2$ is the overbounding variance based on the months of data gathered from multiple globally distributed locations processed in [22]. The error model parameters for MC is assumed to match GNSS, since the difference in satellite motion is already captured in Eq. (3).

3.3. Multipath Error

The multipath error is modeled as a FOGMP, multiplied by the elevation-dependent mapping function given in [33].

$$ \begin{aligned} {}^{i}\mathcal{E}_{M,\phi,k} &= {}^{i}c_{M,k}\, {}^{i}\zeta_{M,\phi,k} \\ {}^{i}\mathcal{E}_{M,\rho,k} &= {}^{i}c_{M,k}\, {}^{i}\zeta_{M,\rho,k} \end{aligned} \tag{6} $$

where the elevation-dependent multipath mapping function is

$$ {}^{i}c_{M,k} = c_{IF}\left(0.13 + 0.53\, e^{\left(-{}^{i}\theta_{k}[\text{deg}]/10\right)}\right) . \tag{7} $$

for carrier-smoothed measurements [34]. Although we are using raw, non-smoothed measurements in this work, we assume that we are sampling frequently enough that we approximate smoothed measurements. The ionosphere-free measurement combination multiplier, c_{IF}, is computed with the equation

$$ c_{IF} = \sqrt{\frac{f_{L1}^4 + f_{L5}^4}{\left(f_{L1}^2 - f_{L5}^2\right)^2}} \tag{8} $$

where f_{L1} and f_{L5} are the frequencies for L1 and L5 respectively. The use of equivalent c_{IF} values for all constellations is a simplifying assumption that can be refined in future work. The GMP term in Eq. (6) for carrier and code measurements are

$$ \begin{aligned} {}^{i}\zeta_{M,\phi,k} &= e^{-T_s/T_M}\, {}^{i}\zeta_{M,\phi,k-1} + \nu_{M,\phi,k} \qquad , \qquad \nu_{M,\phi,k} \sim N\left(0, \sigma_{M,\phi}^2 \left(1 - e^{-2T_s/T_M}\right)\right) \\ {}^{i}\zeta_{M,\rho,k} &= e^{-T_s/T_M}\, {}^{i}\zeta_{M,\rho,k-1} + \nu_{M,\rho,k} \qquad , \qquad \nu_{M,\rho,k} \sim N\left(0, \sigma_{M,\rho}^2 \left(1 - e^{-2T_s/T_M}\right)\right) \end{aligned} . \tag{9} $$

GNSS multipath error has been modeled for automotive applications in [35], where values for the correlation time constant and pseudorange bounding standard deviation can be used as reference. These values were taken into account to get the parameters for GNSS listed in Table 1, where the order of magnitude difference in multipath error between code and carrier is accounted for. For MC, we assume the same GMP variance, and a time constant scaled for LEO orbits [15, 36].

3.4. Receiver Noise Error

Receiver noise is modeled as Gaussian white noise with an elevation-dependent standard deviation, and is computed as

$$ \begin{aligned} {}^{i}\mathcal{E}_{R,\phi,k} &= {}^{i}\nu_{R,\phi,k} \qquad , \qquad {}^{i}\nu_{R,\phi,k} \sim N(0, {}^{i}\sigma_{R,\phi}^2) \\ {}^{i}\mathcal{E}_{R,\rho,k} &= {}^{i}\nu_{R,\rho,k} \qquad , \qquad {}^{i}\nu_{R,\rho,k} \sim N(0, {}^{i}\sigma_{R,\rho}^2) \end{aligned} . \tag{10} $$

Elevation-dependent receiver noise error models are formulated for airborne aircraft using carrier-smoothed code measurements from GNSS in [18]. The effect of receiver noise is assumed to match for GNSS and MC measurements using parameters

$$ {}^{i}\sigma_{R,\rho,k} = c_{IF}\left(0.15 + 0.43\, e^{\left(-{}^{i}\theta_k\,[\mathrm{deg}]/6.9\right)}\right) \tag{11} $$

$$ {}^{i}\sigma_{R,\phi,k} = \left(\frac{1}{100}\right) c_{IF}\left(0.15 + 0.43\, e^{\left(-{}^{i}\theta_k\,[\mathrm{deg}]/6.9\right)}\right) \tag{12} $$

3.5. Accounting for Uncertainty in Error Time Correlation

Using the maximum Markov process time constant does not always produce an upper bound on the estimate error variance [20]. Moreover, experimental data show that measurement time correlation due to ephemeris, multipath, and troposphere errors do not behave like a FOGMP [21, 37, 38]. To address this issue, we use a pair of GMP autocorrelation functions with time constants T_{min} and T_{max} respectively, to bound the unknown autocorrelation, which does not have to be a FOGMP. Langel showed that these autocorrelation functions could be used to guarantee an upper bound on the estimation error variance for a linear estimator [19]. A practical implementation of this positioning error variance bounding method is described in Appendix A. As a preliminary analysis, the range of GMP time constants $[T_{min}, T_{max}]$ is taken to be $[0.8T_\varepsilon, 1.2T_\varepsilon]$, where T_ε is the FOGMP time constant specified in Table 1. The subscript ε denotes E, T, M for ephemeris, troposphere, and multipath errors respectively.

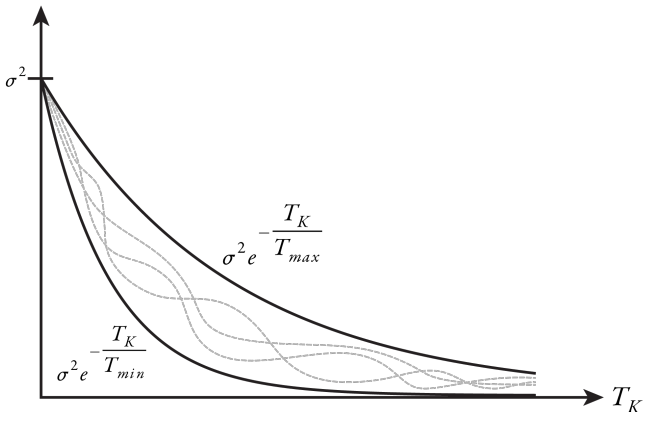

Figure 4: Error Autocorrelation Bounding. This sketch gives a visual representation of how the actual error autocorrelation (gray lines) is bounded by two first order Gauss Markov processes with time constants T_{min} and T_{max} (black lines).

We have refined our models from last year, and in parallel, work is being done to process years of data to get high-integrity error models for these error sources. In future work, we will consider more realistic ranges of values that have recently been published in [21, 22, 32].

3.6. Summary of Error Parameters

The measurement error parameters for ground vehicle applications with PPP corrections are summarized in Table 1. These error models, particularly those of MC will have to be further evaluated using experimental data.

Table 1: Summary of GMP Error Model Parameters

Error Source	Mapping Function	σ_{GMP}	$T_{nominal}$
Ephemeris (GPS)		0.10 m	2 h
Ephemeris (Galileo)		0.10 m	4 h
Ephemeris (MC)		0.10 m	100 min
Troposphere	Eq. (3)	0.05 m	30 min
Code Multipath (GNSS)	Eq. (7)	0.83 m	158 s
Carrier Multipath (GNSS)	Eq. (7)	0.0083 m	158 s
Carrier Multipath (MC)	Eq. (7)	0.0083 m	6 s
Receiver Code Noise (GNSS)		Eq. (11)	
Receiver Carrier Noise		Eq. (12)	

4. GNSS-MC ESTIMATION AND FAULT DETECTION ALGORITHMS

4.1. Batch Measurement Equation

A batch weighted least squares algorithm is used to simultaneously estimate the three-dimensional user position and receiver clock offsets at every time step, and the floating valued carrier phase cycle ambiguities that are constant over time, as long as the carrier is continuously tracked. For practical applications, this method can be implemented sequentially in a sliding window mechanism, as long as adequate receiver memory is available to store current and past measurements. Starting with the linearized measurement

equations for ionosphere-error-free carrier and code measurements Eq. (1), we can derive a batch measurement equation of the form $\mathbf{z} = \mathbf{H}\,\mathbf{x} + \mathbf{v}$ by following the steps detailed in Section 3.1 of [15], and making the following changes:

$$\mathbf{u}_k = \begin{bmatrix} \mathbf{x}_k \\ \tau_{GPS,k} \\ \tau_{Galileo,k} \\ \tau_{MC,k} \end{bmatrix}, \tag{13}$$

$${}^{i}\mathbf{g}_k^{\mathrm{T}} = \begin{bmatrix} -{}^{i}\mathbf{e}_k^{\mathrm{T}} & 1 & 0 & 0 \end{bmatrix} \text{ if satellite } i \text{ is a GPS satellite,} \tag{14}$$

$${}^{i}\mathbf{g}_k^{\mathrm{T}} = \begin{bmatrix} -{}^{i}\mathbf{e}_k^{\mathrm{T}} & 0 & 1 & 0 \end{bmatrix} \text{ if satellite } i \text{ is a Galileo satellite, and} \tag{15}$$

$${}^{i}\mathbf{g}_k^{\mathrm{T}} = \begin{bmatrix} -{}^{i}\mathbf{e}_k^{\mathrm{T}} & 0 & 0 & 1 \end{bmatrix} \text{ if satellite } i \text{ is an MC satellite.} \tag{16}$$

We stack the measurements over time for each satellite i for time instances 1 through q. The resulting geometry matrix, carrier and code measurements, carrier and code measurement noise vectors, and user states are respectively expressed as

$${}^{i}\mathbf{G} = \begin{bmatrix} {}^{i}\mathbf{g}_1^{\mathrm{T}} & & \mathbf{0} \\ & \ddots & \\ \mathbf{0} & & {}^{i}\mathbf{g}_q^{\mathrm{T}} \end{bmatrix} \quad {}^{i}\boldsymbol{\varphi} = \begin{bmatrix} {}^{i}\phi_1 \\ \vdots \\ {}^{i}\phi_q \end{bmatrix} \quad {}^{i}\boldsymbol{\rho} = \begin{bmatrix} {}^{i}\rho_1 \\ \vdots \\ {}^{i}\rho_q \end{bmatrix} \quad {}^{i}\mathbf{v}_\phi = \begin{bmatrix} {}^{i}\nu_{\phi,1} \\ \vdots \\ {}^{i}\nu_{\phi,q} \end{bmatrix} \quad {}^{i}\mathbf{v}_\rho = \begin{bmatrix} {}^{i}\nu_{\rho,1} \\ \vdots \\ {}^{i}\nu_{\rho,q} \end{bmatrix} \quad \mathbf{u} = \begin{bmatrix} \mathbf{u}_1 \\ \vdots \\ \mathbf{u}_q \end{bmatrix}. \tag{17}$$

The measurements get stacked with GNSS carrier phase measurements first, followed by MC carrier phase measurements, then GNSS code measurements. The resulting stack of measurements is

$$\begin{bmatrix} {}^{1}\boldsymbol{\varphi} \\ {}^{2}\boldsymbol{\varphi} \\ \vdots \\ {}^{n_{sat}}\boldsymbol{\varphi} \\ {}^{1}\boldsymbol{\rho} \\ {}^{2}\boldsymbol{\rho} \\ \vdots \\ {}^{n_{GNSS}}\boldsymbol{\rho} \end{bmatrix} = \begin{bmatrix} {}^{1}\mathbf{G} & \mathbf{1}_{q\times 1} & 0 & & 0 \\ {}^{2}\mathbf{G} & 0 & \mathbf{1}_{q\times 1} & & 0 \\ \vdots & \vdots & \vdots & \ddots & \vdots \\ {}^{n_{sat}}\mathbf{G} & 0 & 0 & & \mathbf{1}_{q\times 1} \\ {}^{1}\mathbf{G} & 0 & 0 & & 0 \\ {}^{2}\mathbf{G} & 0 & 0 & & 0 \\ \vdots & \vdots & \vdots & \ddots & \vdots \\ {}^{n_{GNSS}}\mathbf{G} & 0 & 0 & & 0 \end{bmatrix} \begin{bmatrix} \mathbf{u} \\ {}^{1}\eta \\ {}^{2}\eta \\ \vdots \\ {}^{n_{sat}}\eta \end{bmatrix} + \begin{bmatrix} {}^{1}\mathbf{v}_\phi \\ {}^{2}\mathbf{v}_\phi \\ \vdots \\ {}^{n_{sat}}\mathbf{v}_\phi \\ {}^{1}\mathbf{v}_\rho \\ {}^{2}\mathbf{v}_\rho \\ \vdots \\ {}^{n_{GNSS}}\mathbf{v}_\rho \end{bmatrix} \tag{18}$$

where n_{GNSS} is the number of GNSS satellites, and n_{sat} is the total number of visible satellites. The stack of measurements can be compactly written as

$$\begin{bmatrix} \boldsymbol{\varphi} \\ \boldsymbol{\rho} \end{bmatrix} = \begin{bmatrix} \mathbf{G}_\phi & \mathbf{H}_N \\ \mathbf{G}_\rho & \mathbf{0} \end{bmatrix} \begin{bmatrix} \mathbf{u} \\ \boldsymbol{\eta} \end{bmatrix} + \begin{bmatrix} \mathbf{v}_\phi \\ \mathbf{v}_\rho \end{bmatrix}. \tag{19}$$

The batch measurement error covariance matrix accounting for measurement error time correlation is given by

$$\mathbf{V} = \begin{bmatrix} \mathbf{V}_E + \mathbf{V}_T & \mathbf{V}_E + \mathbf{V}_T \\ \mathbf{V}_E + \mathbf{V}_T & \mathbf{V}_E + \mathbf{V}_T \end{bmatrix} + \begin{bmatrix} \mathbf{V}_{\phi\phi,M} + \mathbf{V}_{\phi\phi,R} & \mathbf{0} \\ \mathbf{0} & \mathbf{V}_{\rho\rho,M} + \mathbf{V}_{\rho\rho,R} \end{bmatrix} \tag{20}$$

where $\mathbf{V}_E$ is the ephemeris error covariance, $\mathbf{V}_T$ is the residual tropospheric error covariance, $\mathbf{V}_M$ is the multipath error covariance, and $\mathbf{V}_R$ is the receiver noise error covariance. The covariance matrix captures the fact that $\mathbf{V}_E$ and $\mathbf{V}_T$ are common to code and carrier measurements, while $\mathbf{V}_M$ and $\mathbf{V}_R$ are different for code and carrier measurements. For each satellite i these covariances are

$${}^{i}\mathbf{V}_E = \sigma_E^2 \exp\left(-\frac{T_s}{T_E}\mathbf{B}\right),$$

$${}^{i}\mathbf{V}_T = \sigma_T^2\, {}^{i}\mathbf{c}_T\, {}^{i}\mathbf{c}_T^{\mathrm{T}} \circ \exp\left(-\frac{T_s}{T_T}\mathbf{B}\right), \quad {}^{i}\mathbf{V}_R = \begin{bmatrix} {}^{i}\sigma_{R,1}^2 & 0 & \dots & 0 \\ 0 & {}^{i}\sigma_{R,2}^2 & \ddots & \vdots \\ \vdots & \ddots & \ddots & 0 \\ 0 & \dots & 0 & {}^{i}\sigma_{R,q}^2 \end{bmatrix}, \text{ where } \mathbf{B} = \begin{bmatrix} 0 & 1 & 2 & \dots & q-1 \\ 1 & 0 & 1 & & \vdots \\ 2 & 1 & 0 & & \\ \vdots & & & \ddots & \\ q-1 & & & & 0 \end{bmatrix}.$$

$${}^{i}\mathbf{V}_M = \sigma_M^2\, {}^{i}\mathbf{c}_M\, {}^{i}\mathbf{c}_M^{\mathrm{T}} \circ \exp\left(-\frac{T_s}{T_M}\mathbf{B}\right), \tag{21}$$

The matrix **B** is a Toeplitz matrix. The symbol "$\circ$" indicates element-by-element multiplication of matrices, where as "exp $\circ$" means element-wise exponential function applied to the matrix in parentheses. For error source ε, σ_ε is the GMP standard deviation, ${}^{i}\mathbf{c}_\varepsilon$ is the vector of elevation-dependent coefficients stacked at all times for satellite i, T_ε is the Markov process correlation time constant, and T_s is the sampling interval. The matrix **B** arises from computing the cross-correlation terms between separate times whilst having a fixed sampling period. The detailed derivation of these time-correlated measurement error covariance matrices is described in the Appendix of [15].

4.2. Batch Estimator

The weighted least squares estimate $\hat{\mathbf{x}}$ that minimizes the sum of squares of the weighted observation errors is given as

$$\hat{\mathbf{x}} = \mathbf{S}\mathbf{z} \tag{22}$$

where we define the weighting matrix as $\mathbf{W} = \mathbf{V}^{-1}$ to get the estimator matrix

$$\mathbf{S} = \left(\mathbf{H}^{\mathrm{T}}\mathbf{W}\mathbf{H}\right)^{-1}\mathbf{H}^{\mathrm{T}}\mathbf{W}. \tag{23}$$

4.3. Detection Using Multiple Hypothesis Solution Separation

Fault detection is implemented using a multiple hypothesis solution separation (MHSS) batch ARAIM method [39, 40, 18, 41, 42]. We consider a set of mutually exclusive, exhaustive hypothesis $H^{(i)}$ for fault modes $i = 0, 1, \ldots, h$, where the number of hypotheses h is discussed in Section 4.4. The right superscript "(i)" for hypothesis index is not be confused with the left superscript "i" for satellite index. Under each hypothesis, a subset of satellites is assumed to be impacted by the fault, and the fault-tolerant subset solution for $H^{(i)}$ excludes measurements from the faulted satellites. We consider fault-free $H^{(0)}$, and faulted hypotheses $H^{(\geq 1)}$. The fault-tolerant position solution for each hypothesis is defined as

$$\hat{\mathbf{x}}^{(i)} = \mathbf{S}^{(i)}\mathbf{z} \tag{24}$$

$$\mathbf{S}^{(i)} = \left(\mathbf{H}^{(i)^{\mathrm{T}}}\mathbf{W}^{(i)}\mathbf{H}^{(i)}\right)^{-1}\mathbf{H}^{(i)^{\mathrm{T}}}\mathbf{W}^{(i)} \tag{25}$$

where $\mathbf{S}^{(i)}$ is the estimator which excludes measurements from the faulted satellite/s for hypothesis $H^{(i)}$. Given this hypothesis' estimator, the corresponding estimation error variance for the user position at current time q for the North component is given by

$$\sigma_N^{(i)^2} = \left(\mathbf{H}^{(i)^{\mathrm{T}}}\mathbf{W}^{(i)}\mathbf{H}^{(i)}\right)^{-1}_{(q_N, q_N)} \tag{26}$$

where q_N is the index for the current time user position North component. The variance is similarly derived for the East and Down position components, designated by E and D subscripts. We define the solution separation between the all-in-view and fault-tolerant position solutions as

$$\Delta\hat{\mathbf{x}}^{(i)} = \hat{\mathbf{x}}^{(i)} - \hat{\mathbf{x}}^{(0)} = \left(\mathbf{S}^{(i)} - \mathbf{S}^{(0)}\right)\mathbf{z} \tag{27}$$

from which we can extract the solution separation components $\Delta\hat{x}_N^{(i)}$, $\Delta\hat{x}_E^{(i)}$, and $\Delta\hat{x}_D^{(i)}$, which are normally distributed with variances $\sigma_{\Delta,N}^{(i)^2}$, $\sigma_{\Delta,E}^{(i)^2}$, and $\sigma_{\Delta,D}^{(i)^2}$ respectively. These solution separation variances are used in defining the detection thresholds in the next section. Nominal biases, which are included in standalone solutions [39, 40, 18] and may or may not impact PPP corrected signals, will be addressed in future work.

4.4. Integrity and Continuity Risk Evaluation

We write the integrity risk, or probability of hazardously misleading information (HMI) considering all fault hypothesis as

$$P_{HMI} = \sum_{i=0}^{2^n-1} P\left(HMI|H^{(i)}\right)P_{H^{(i)}} \tag{28}$$

where n is the sum of the number of visible satellites and the number of constellations, 2^n is the total number of faulted versus fault-free subset combinations in the set n, $H^{(i)}$ are the fault and fault-free hypotheses, $P_{H^{(i)}}$ is the prior probability of $H^{(i)}$ occurrence, and HMI occurs when the estimation error on the state of interest exceeds a predetermined threshold and is not detected. Going through all possible hypotheses is computationally expensive so in practice, the hypotheses are divided into two groups: one containing faults

that are most likely to occur and whose impact on estimation error we want to monitor, and one containing unlikely hypotheses which we will not monitor, but will account for considering its prior probability of occurrence. We require that the integrity risk contribution from the not monitored hypotheses be significantly smaller than the integrity risk requirement. Thus, Eq. (28) can be bounded by [41]

$$P_{HMI} \leq \sum_{i=0}^{h} P\left(HMI|H^{(i)}\right) P_{H^{(i)}} + \left(1 - \sum_{i=0}^{h} P_{H^{(i)}}\right) \tag{29}$$

where the first term is the integrity risk for all monitored hypotheses (fault-free and faulted), and the second term is the bound on integrity risk for hypotheses not monitored. The first term in Equation (29) can be rewritten as the sum of risk contributions from the North, East, and Down directions as follows

$$P_{HMI} \leq \sum_{i=0}^{h} P\left(HMI_N|H^{(i)}\right) P_{H^{(i)}} + \sum_{i=0}^{h} P\left(HMI_E|H^{(i)}\right) P_{H^{(i)}} + \sum_{i=0}^{h} P\left(HMI_D|H^{(i)}\right) P_{H^{(i)}} + \left(1 - \sum_{i=0}^{h} P_{H^{(i)}}\right) \tag{30}$$

where subscripts N, E, D denote North, East, Down respectively. The integrity risk in the Down direction is

$$\sum_{i=0}^{h} P\left(HMI_D|H^{(i)}\right) P_{H^{(i)}} = P\left(\left|\epsilon_D^{(0)}\right| > VAL \mid H^{(0)}\right) P_{H^{(0)}} + \sum_{i=1}^{h} P\left(\left|\epsilon_D^{(i)}\right| + T_D^{(i)} > VAL \mid H^{(i)}\right) P_{H^{(i)}}. \tag{31}$$

where $\epsilon_D^{(0)}$ is the Down component of the error for the all-in-view position solution, $H^{(0)}$ is the fault-free hypothesis, $\epsilon_D^{(i)}$ is the Down component of the error for the fault-tolerant position solution, $H^{(i)}$ is the ith hypothesis, VAL is the vertical alert limit that defines hazardous situations, and $T_D^{(i)}$ is the Down component detection threshold for the ith test, based on a predefined continuity risk requirement allocation that limits the probability of false alarms [18]. We compute the thresholds $T_D^{(i)}$, using the equation

$$T_D^{(i)} = Q^{-1}\left(\frac{C_{\text{req}}}{2h}\right) \sigma_{\Delta,D}^{(i)}. \tag{32}$$

The horizontal alert limit is defined by a circle of radius equal to HAL centered at the estimated user position in the North-East plane as shown in Figure 5. The horizontal positioning error at current time for hypothesis (i) is represented by a covariance ellipse centered on the mean horizontal position error. The horizontal integrity risk is the integral of the bivariate probability density function over the area outside the HAL circle. Evaluating this integral can be quite complex, so in practice, it is approximated using different methods [43, 44]. In this work, we conservatively account for the integrity risk in the North and East direction by considering a square inscribed in the HAL circle. The perpendicular distance from the origin to any side of the square is $HAL/\sqrt{2}$. We calculate the integrity risk in the North direction as follows

$$\sum_{i=0}^{h} P\left(HMI_N|H^{(i)}\right) P_{H^{(i)}} \leq P\left(\left|\epsilon_N^{(0)}\right| > \frac{HAL}{\sqrt{2}} \mid H^{(0)}\right) P_{H^{(0)}} + \sum_{i=1}^{h} P\left(\left|\epsilon_N^{(i)}\right| + T_N^{(i)} > \frac{HAL}{\sqrt{2}} \mid H^{(i)}\right) P_{H^{(i)}} \tag{33}$$

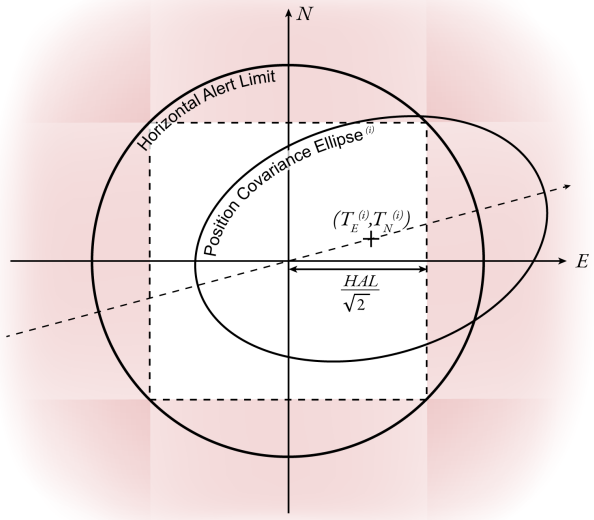

Figure 5: Square Inscribed in the HAL Circle. The shaded region is the upper bound on the horizontal integrity risk.

where the positioning error $\epsilon_N^{(i)}$ is assumed to be normally distributed with variance $\sigma_N^{(i)^2}$, and mean equal to the North component detection threshold $T_N^{(i)}$, computed as

$$T_N^{(i)} = Q^{-1}\left(\frac{C_{\text{req}}}{4h}\right) \sigma_{\Delta,N}^{(i)}. \tag{34}$$

The integrity risk and detection thresholds for the East direction are calculated the same way. The total integrity risk is the sum of risk contributions from the North, East, and Down directions, and the contributions from the hypotheses not monitored.

4.5. Modified Estimator to Reduce Integrity Risk

The weighted least squares estimator minimizes the all-in-view position solution estimation error variance under fault-free conditions. However, this solution is typically not the one that minimizes the integrity risk considering fault hypotheses. When P_{HMI} exceeds the integrity risk requirement, the objective of the modified estimator is to choose a position solution that minimizes the total integrity risk. The effect is that we trade off a reduction in accuracy for an increase in integrity. This manifests in an increase in $\sigma^{(0)}$, which changes the values for $\sigma_{\Delta}^{(i)}$, and has the overall effect of decreasing the second term on the right hand side of Eq. (??). The implementation of this modified estimator follows the algorithm described in [18], which we implement here for a batch of measurements over time. The modified estimator does not consider the prior rates of fault when determining which subset solution to deweight, so we exclude less likely faults as candidates for modifying the estimator. Note that under the configurations selected, the optimal estimator has negligible effects on the integrity risk.

4.6. Number of Effectively Independent Samples

We reconcile the instantaneous integrity risk in Eq (29), with the operational integrity requirement which is specified per hour, by defining the number of effectively independent samples, N_{ES}. This method was developed in [45] to rigorously account for the added integrity risk arising from multiple exposures to hazardously misleading events, and multiple detection tests over the exposure period. The modified integrity risk equation based on Eq. (29)is

$$P_{HMI}(T_{EXP}) \leq \sum_{i=0}^{h} P\left(HMI|H^{(i)}\right) N_{ES,H^{(i)}} P_{H^{(i)}} + \left(1 - \sum_{i=0}^{h} P_{H^{(i)}}(T_{EXP})\right). \tag{35}$$

For the first term in Eq. (35) corresponding to monitored hypotheses, the bound on $N_{ES,H^{(i)}}$ is defined as [45]

$$N_{ES,H^{(i)}} = \left(\frac{T_{EXP,int}}{TTA}\right) \tag{36}$$

where $T_{EXP,int}$ is the period of operation defined for integrity, and TTA is the required time-to-alert (maximum allowable elapsed time from HMI onset until a system alert). As for the hypotheses not monitored, the last term in parenthesis in Eq. (35), the prior probability of $H^{(i)}$ occurrence, $P_{H^{(i)}}$, is modified to use the prior probability of a fault event given by

$$P_{event,i}(T_{EXP}) = \left(1 + \frac{T_{EXP,int}}{MTTN_i}\right) P_{event,i} \tag{37}$$

where $MTTN$ is the mean-time-to-notify (commitment made by the service provider for the time elapsed between when a fault is detected at the ground, to when the user is notified of the fault), and $P_{event,i}$ denotes $P_{sat,i}$ for a fault on satellite i, and $P_{const,i}$ for a wide fault on constellation i. We assume that $MTTN$ is 1 h for all fault events on all constellations. An example computation of $P_{H^{(i)}}(T_{EXP})$ using Eq. (37) is given in Appendix B. Furthermore, the detection thresholds in Eq. (32) and Eq. (34) are modified to

$$T_D^{(i)} = Q^{-1}\left(\frac{C_{\text{req}}}{2hN_{ES,cont}}\right)\sigma_{\Delta,D}^{(i)} \quad , \quad T_{N/E}^{(i)} = Q^{-1}\left(\frac{C_{\text{req}}}{4hN_{ES,cont}}\right)\sigma_{\Delta,N}^{(i)} \tag{38}$$

where

$$N_{ES,cont} = \frac{T_{EXP,cont}}{TTA} \tag{39}$$

and $T_{EXP,cont}$ is the period of operation defined for continuity. The values for these parameters are defined in Table 2.

5. IMPACT OF CASCADING FAULTS

Given that a GNSS fault can cascade to a constellation-wide fault on MC, the spaceborne receiver's detection capability is a driving factor to the overall integrity at the ground user. In this section, we derive the equations that would allow us to determine the spaceborne receiver detection capability required to bring about an improvement in MC-augmented GNSS integrity. We first look at the case for GNSS only. We compute P_{HMI} at the ground receiver considering mutually exclusive, exhaustive hypotheses of GNSS fault-free conditions (FF,G), and GNSS fault conditions (G).

$$P(HMI_G) = P\left(HMI_G, H_{FF,G}\right)P_{FF,G} + P\left(HMI_G, H_G\right)P_G \tag{40}$$

Then we add MC satellites, and make the assumption that a GNSS fault always causes a constellation-wide fault on all MC satellites visible at a given user location. This assumption is approximate but conservative. The resulting P_{HMI} equation considers hypotheses of FF (FF,GM), GNSS faults that always cause MC wide fault (G), and other narrow and wide MC faults (M). Under these assumptions, we get

$$P\left(HMI_{GM}\right) \leq P\left(HMI_{GM}, H_{FF,GM}\right) P_{FF,GM} + P\left(HMI_{GM}, H_{G}\right) P_{G} + P\left(HMI_{GM}, H_{M}\right) P_{M}\,. \tag{41}$$

We compare the terms in Eq. (41) to the terms in the GNSS-only case in Eq. (40). For the first term, we have proven in [15] that the FF term for GNSS-MC is less than the FF term for GNSS-only, which pleads in favor of adding MC. The second term in Eq. (41) appears similar to that of GNSS-only, but we show in Appendix C that it is actually larger because the false alarm risk has to be allocated to more hypothesis with the addition of MC. Lastly, the third term in Eq. (41) has no counter part in the GNSS-only case which pleads against adding MC. The details of this comparison are in Appendix C. Typically, in RAIM and ARAIM, the FF term does not dominate the integrity risk equation (not by orders of magnitude). Our analysis supports this idea, and has consistently shown that the first term is insufficient to compensate for the impact of the latter two. Under these assumptions, MC-augmentation would always degrade integrity.

We can mitigate this effect by incorporating spaceborne integrity monitoring. Using spaceborne MC RAIM, the second right-hand-side term in Eq. (41) is split into two: one that accounts for just GNSS faults (G), and one that accounts for MC-wide faults caused by GNSS faults not detected at the spaceborne receiver (MW). At the ground receiver, we now have

$$P\left(HMI_{GM}\right) \leq P\left(HMI_{GM}, H_{FF,GM}\right) P_{FF,GM} + P\left(HMI_{GM}, H_{G}\right) P_{G} + P\left(HMI_{GM}, H_{MW}\right) P_{G} P_{SFD} + P\left(HMI_{GM}, H_{M}\right) P_{M} \tag{42}$$

where the probability of spaceborne failed detection, P_{SFD}, will determine the conditions where MC-augmentation improves or degrades integrity. The sensitivity analysis on P_{SFD} is discussed in a subsequent section.

6. INTEGRITY PERFORMANCE ANALYSIS

6.1. Covariance Analysis Implementation

The nominal configuration uses a 10-minute batch, with measurements sampled every 30 seconds [15]. The 10-minute batch is performed repeatedly at regular 1-minute intervals over 24 hours at a reference location in Memphis, Tennessee (35°N 90°W 0m altitude), where we found the worst-case mid-latitude GNSS positioning performance. The batch period and measurement sampling rate were chosen to take full advantage of MC satellite motion, and ensure that we are sampling frequently enough to average out random errors.

Table 2: List of Constants Used in Detector

	Description	Value
I_{req}	total integrity budget	10^{-6}/h [2]
C_{req}	continuity risk requirement to limit probability of false alarms	10^{-5} [2]
P_{sat}	probability of single satellite fault (GPS, Galileo, MC)	10^{-5}, 10^{-5}, 10^{-5} [18]
P_{const}	probability of constellation fault (GPS, Galileo, MC)	10^{-8}, 10^{-8}, 10^{-7} [18, 46]
P_{SFD}	probability of failed detection at the spaceborne MC receiver (range of values)	$1, 10^{-1}, 10^{-2}$
VAL	vertical alert limit	2.50 m [1, 2, 3]
HAL	horizontal alert limit	1.50 m [1, 2, 3]
$T_{EXP,int}$	exposure time for integrity	1 hr [2]
$T_{EXP,cont}$	exposure time for continuity	15 s [2]
TTA	time-to-alert	10 s [2]
$MTTN$	mean-time-to-notify	1 h [18, 45, 46]

6.2. Performance Sensitivity to the Probability of Failed Spaceborne Detection

The conditions where MC-augmentation improves or degrades integrity depends on the probability of failed detection (P_{SFD}) at the MC spaceborne receiver. To analyze this, we perform a sensitivity analysis at the example Memphis location, where we compare the availability values at the reference location as we vary P_{SFD}. The integrity risk over time for GNSS only is shown as the black line in Figure 6, and for this sample location, GNSS availability is 81.12%. Availability is the percentage of time over 24 hours where the integrity risk is below the requirement, shown as the horizontal dashed line. With MC-augmentation at $P_{SFD} = 1$, there is no integrity

monitoring at the MC spaceborne receiver, and we get the dotted gray line with GNSS-MC availability of 34.63%. In this case, GNSS-MC degrades integrity as compared to GNSS only. If we decrease this probability of no spaceborne detection to 0.1, we get the dark gray line with GNSS-MC availability of 85.98%. At this P_{SFD}, GNSS-MC already improves integrity with respect to GNSS only. We consider a better detector by decreasing P_{SFD} further to 0.001, and get the blue line where GNSS-MC is available 100% of the time for this reference location. The performance of GNSS-MC is not only time-dependent, but also location-dependent. So we take 0.001 as the value of P_{SFD} for the MC spaceborne detector, and continue to do a performance analysis for a worlwide grid of locations.

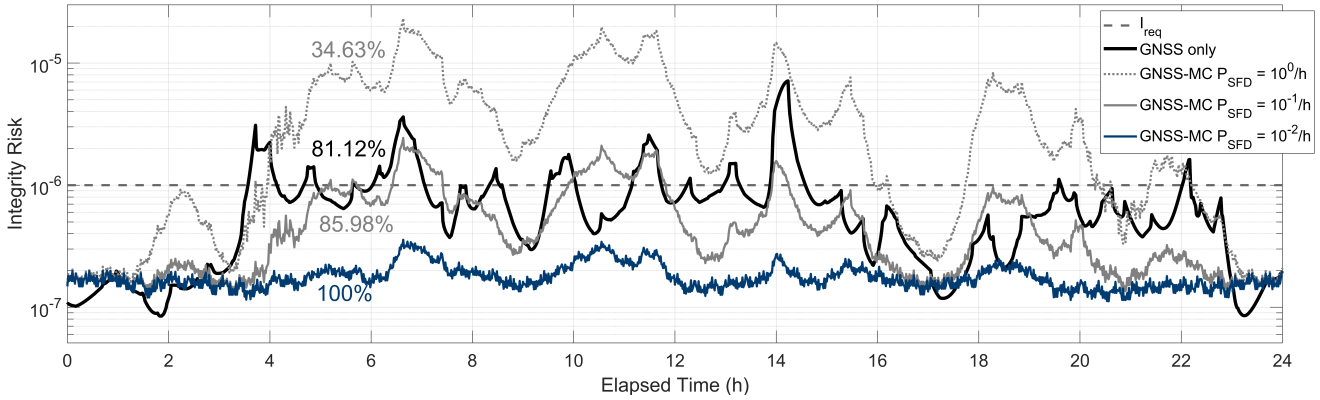

Figure 6: Integrity risk over time at a reference location for GNSS only, and GNSS-MC at varying probability of failed GNSS fault detection at the spaceborne MC receiver (P_{SFD})

6.3. Global Availability Analysis

The performance of GNSS only is on the left of Figure 7. We clearly see an improvement in integrity with the image on the right of Figure 7 for MC-augmented GNSS, where we have less lighter regions, and more blue. A comparison can also be made for coverage. The coverage, defined here as the percentage of locations where we have 95% availability is 33.76% for GNSS. This means that around 34% of locations get at least 95% GNSS availability for this simulation configuration. This coverage is increased to 82.49% with MC-augmented-GNSS.

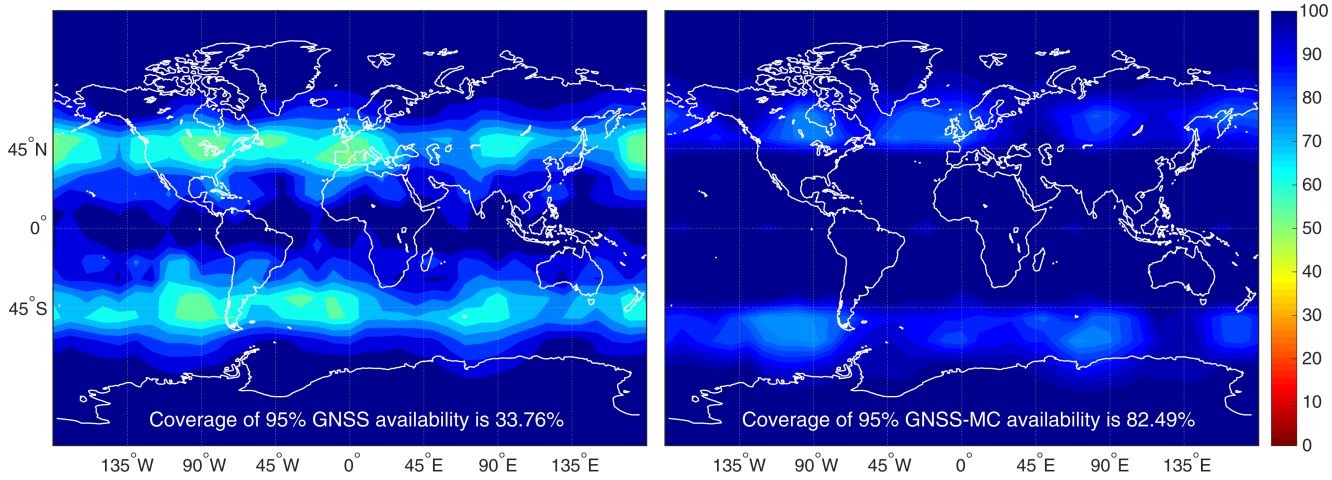

Figure 7: Availability map of GNSS and GNSS-MC. The availability maps show the integrity performance using GNSS only (left plot) and GNSS-MC (right plot). Ten minute batches are simulated at regular ten minute intervals over 24 hours for a 10° × 10° grid of locations. Each grid point is assigned a color that represents the availability value given by the color bar on the right. For coverage results shown with white text, each grid point's availability is scaled by the cosine of the latitude. This accounts for the fact that grid points are taken at regular latitude intervals, but they represent different areas at low versus high latitude locations.

7. CONCLUSIONS

In this paper, we quantified integrity for a GNSS-MC-PPP system using GPS, Galileo, and a Starlink-like MC. An algorithm was developed using dual-frequency, multi-constellation Advanced Receiver Autonomous Integrity Monitoring (ARAIM), but incorporating measurements over time. Robust models of measurement error time correlation were included as well. A GNSS-MC-PPP system architecture is defined based on the existing GNSS-PPP architecture. Given that GNSS faults can cascade to constellation-wide MC faults in the proposed architecture, the sensitive parameter defining the conditions where GNSS-MC improves integrity is derived using the integrity risk equations. A sensitivity analysis was implemented at an example user location to investigate the effect of cascading faults on GNSS-MC integrity, by varying the probability of failed spaceborne detection at the MC receiver. This analysis identified the need for a layer of integrity monitoring at the MC spaceborne receiver, in addition to integrity monitoring at the ground user, and ground control segment.

Appendix A. ERROR AUTOCORRELATION BOUNDING

We first define the estimator vector

$$\mathbf{s}_u = \left[\boldsymbol{\alpha}_u^{\mathrm{T}}\mathbf{S}\right]_{1\times N} \tag{43}$$

where subscript u can stand for the North, East, and Down directions, and $\mathbf{S}$ is the estimator matrix that uses the maximum time constants for the error models used in $\mathbf{V}$. The first term $\boldsymbol{\alpha}_u^{\mathrm{T}}$ is a row vector of length equal to the number of states, composed of zeros except for the element corresponding to the uth position state at current time. We rewrite the estimation error variance for the uth position using an equivalent expression [19]

$$\sigma_u^2 = \sum_{i=1}^{N}\sum_{j=1}^{N}[\mathbf{M}\circ\mathbf{V}]_{i,j} \tag{44}$$

where $\mathbf{M} = \left[\mathbf{s}_u^{\mathrm{T}}\mathbf{s}_u\right]_{N\times N}$, and the symbol "$\circ$" represents element-wise matrix multiplication. We derive a practical way to implement the method in [19]. Following the method in [19], we add up the variance contributions in the worst-conspiring manner using the following equations.

$$\sigma_+^2 = \sum_{i=1}^{N}\sum_{j=1}^{N}[\mathbf{M}_+\circ\mathbf{V}(T_{max})]_{i,j} \qquad \text{where} \qquad [\mathbf{M}_+]_{i,j} = \begin{cases}\left[\mathbf{s}_u^{\mathrm{T}}\mathbf{s}_u\right]_{i,j} \text{ if } \left[\mathbf{s}_u^{\mathrm{T}}\mathbf{s}_u\right]_{i,j} \geq 0\\ 0 \quad \text{otherwise}\end{cases} \tag{45}$$

$$\sigma_-^2 = \sum_{i=1}^{N}\sum_{j=1}^{N}[\mathbf{M}_-\circ\mathbf{V}(T_{min})]_{i,j} \qquad \text{where} \qquad [\mathbf{M}_-]_{i,j} = \begin{cases}\left[\mathbf{s}_u^{\mathrm{T}}\mathbf{s}_u\right]_{i,j} \text{ if } \left[\mathbf{s}_u^{\mathrm{T}}\mathbf{s}_u\right]_{i,j} < 0\\ 0 \quad \text{otherwise}\end{cases} \tag{46}$$

$$\sigma_{u,b}^2 = \sigma_+^2 + \sigma_-^2 \geq \sigma_u^2 \tag{47}$$

where $\sigma_{u,b}^2$ is the bound on the variance produced by simply using the maximum time constants in $\mathbf{V}$.

Appendix B. EXAMPLE $P_{H^{(i)}}$ CALCULATION FOR HYPOTHESES NOT MONITORED

We want to determine the prior probability of $H^{(i)}$ occurrence that accounts for the number of independent samples. For example, hypothesis $i = 1$ corresponding to a fault on satellite 1 and no other faults could be expressed as

$$P_{H^{(1)}}(T_{EXP}) = P_{sat,1}(T_{EXP})\prod_{i=2}^{n_{sat}}\left(1 - P_{sat,i}(T_{EXP})\right)\prod_{j=1}^{n_{const}}\left(1 - P_{const,j}(T_{EXP})\right) \tag{48}$$

where $P_{sat,i}(T_{EXP})$ and $P_{const,j}(T_{EXP})$ are computed following Eq. (37) to get

$$P_{sat,i}(T_{EXP}) = \left(1 + \frac{T_{EXP,int}}{MTTN_{sat,i}}\right)P_{sat,i} \quad , \quad P_{const,j}(T_{EXP}) = \left(1 + \frac{T_{EXP,int}}{MTTN_{const,j}}\right)P_{const,j} \tag{49}$$

using the values for $P_{sat,i}$ and $P_{const,j}$ given in Table 2.

Appendix C. COMPARISON BETWEEN $P(HMI_G)$ AND $P(HMI_{GM})$

We show the comparison between terms in Eq. (41) and terms in the GNSS-only case in Eq. (40). For the first term, we know that $P_{FF,G} \geq P_{FF,GM}$, and have proven in [15] that

$$P\left(HMI_G, H_{FF,G}\right) \geq P\left(HMI_{GM}, H_{FF,GM}\right) \tag{50}$$

therefore, this first contribution pleads in favor of adding MC. The third term in Eq. (41) has no counterpart in the GNSS-only case, and

$$P\left(HMI_{GM}, H_M\right) P_M \geq 0 \tag{51}$$

therefore this contribution pleads against adding MC. For the second terms in Eq. (41)-(42), we can show that

$$P\left(HMI_G, H_G\right) \leq P\left(HMI_{GM}, H_G\right) \tag{52}$$

in three steps. First, using multiple hypothesis solution separation,

$$P\left(HMI_G, H_G\right) \leq P\left(|\epsilon_G| + k_{FA,G}\,\sigma_{\Delta,G} > AL\right) P_G \tag{53}$$

where ϵ_G is the subset solution excluding all faulted GNSS SVs, $k_{FA,G}$ is the false alarm probability multiplier, and

$$\sigma_{\Delta,G} \equiv \sqrt{\sigma_G^2 - \sigma_{0,G}^2} \tag{54}$$

with σ_G^2 the variance of ϵ_G and $\sigma_{0,G}^2$ the variance of the full-set solution including all GNSS satellites. In parallel,

$$P\left(HMI_{GM}, H_G\right) \leq P\left(|\epsilon_G| + k_{FA,GM}\,\sigma_{\Delta,GM} > AL\right) P_G \tag{55}$$

where ϵ_G is still the same subset solution excluding all faulted GNSS SVs and all MC SVs, $k_{FA,G}$ is a different false alarm probability multiplier, and

$$\sigma_{\Delta,GM} \equiv \sqrt{\sigma_G^2 - \sigma_{0,GM}^2} \tag{56}$$

with σ_G^2 still the variance of ϵ_G and $\sigma_{0,GM}^2$ the variance of the full-set solution including all GNSS and MC satellites. Finally, we have

$$\sigma_{\Delta,G} \leq \sigma_{\Delta,GM} \quad \text{because} \quad \sigma_{0,G}^2 \geq \sigma_{0,GM}^2, \quad \text{and} \quad k_{FA,G} \leq k_{FA,GM} \tag{57}$$

because there are more hypotheses between which the false alarm risk requirement must be allocated. Thus,

$$k_{FA,G}\,\sigma_{\Delta,G} \leq k_{FA,GM}\,\sigma_{\Delta,GM} \tag{58}$$

and

$$P\left(|\epsilon_G| + k_{FA,G}\,\sigma_{\Delta,G} > AL\right) P_G \leq P\left(|\epsilon_G| + k_{FA,GM}\,\sigma_{\Delta,GM} > AL\right) P_G \tag{59}$$

therefore this contribution pleads against adding MC.

References

[1] T. G. Reid, S. E. Houts, R. Cammarata, G. Mills, S. Agarwal, A. Vora, and G. Pandey, "Localization Requirements for Autonomous Vehicles," *SAE International Journal of Connected and Automated Vehicles*, vol. 2, no. 3, pp. 1–16, 2019.

[2] M. Joerger, S. Pullen, R. Capua, and SC-134 WG1-Automotive, "Integrity Message Development and Harmonization," in *RTCM Meeting*, May 2020.

[3] K. Gunning, J. Blanch, T. Walter, L. de Groot, and L. Norman, "Design and Evaluation of Integrity Algorithms for PPP in Kinematic Applications," *Proceedings of the 31st International Technical Meeting of the Satellite Division of the Institute of Navigation, ION GNSS+ 2018*, pp. 1910–1939, 2018.

[4] L. Norman, E. Infante, and L. De Groot, "Integrity Performance for Precise Positioning in Automotive," *Proceedings of the 32nd International Technical Meeting of the Satellite Division of the Institute of Navigation, ION GNSS+ 2019*, pp. 1653–1663, 2019.

[5] B. Pervan, *Navigation Integrity for Aircraft Precision Landing Using the GPS*. PhD thesis, Stanford University, 1996.

[6] B. W. Remondi, "Pseudo-Kinematic GPS Results Using the Ambiguity Function Method," in *46th Annual Meeting of the Institute of Navigation*, (Atlantic City, NJ), pp. 41–49, 1990.

[7] R. J. Danchik, "An Overview of Transit Development," *Johns Hopkins APL Technical Digest (Applied Physics Laboratory)*, vol. 19, no. 1, pp. 18–26, 1998.

[8] M. Rabinowitz, B. W. Parkinson, C. E. Cohen, M. L. O'Connor, and D. G. Lawrence, "A System Using LEO Telecommunication Satellites for Rapid Acquisition of Integer Cycle Ambiguities," in *IEEE 1998 Position Location and Navigation Symposium*, (Palm Springs, CA, USA), pp. 137–145, 1998.

[9] M. Joerger, J. Neale, B. Pervan, and S. Datta-Barua, "Measurement Error Models and Fault-Detection Algorithms for Multi-Constellation Navigation Systems," in *IEEE/ION Position, Location and Navigation Symposium*, pp. 927–946, 2010.

[10] C. T. Ardito, J. J. Morales, J. J. Khalife, A. A. Abdallah, and Z. M. Kassas, "Performance Evaluation of Navigation using LEO Satellite Signals with Periodically Transmitted Satellite Positions," in *ION 2019 International Technical Meeting Proceedings*, pp. 306–318, 2019.

[11] L. Wang, R. Chen, D. Li, G. Zhang, X. Shen, B. Yu, C. Wu, S. Xie, P. Zhang, M. Li, and Y. Pan, "Initial Assessment of the LEO Based Navigation Signal Augmentation System from Luojia-1A Satellite," *Sensors (Switzerland)*, vol. 18, no. 11, 2018.

[12] T. G. Reid, A. M. Neish, T. Walter, and P. K. Enge, "Broadband LEO Constellations for Navigation," *Navigation, Journal of the Institute of Navigation*, vol. 65, no. 2, pp. 205–220, 2018.

[13] H. Ge, B. Li, M. Ge, N. Zang, L. Nie, Y. Shen, and H. Schuh, "Initial Assessment of Precise Point Positioning with LEO Enhanced Global Navigation Satellite Systems (LeGNSS)," *Remote Sensing*, vol. 10, no. 7, 2018.

[14] M. L. Psiaki, "Navigation using Carrier Doppler Shift from a LEO Constellation : TRANSIT on Steroids," in *33rd International Technical Meeting of The Satellite Division of the Institute of Navigation, ION GNSS+ 2020*, 2020.

[15] D. Racelis, M. Joerger, and B. Pervan, "Fault-Free Integrity Analysis of Mega-Constellation-Augmented GNSS," in *32nd International Technical Meeting of the Satellite Division of the Institute of Navigation, ION GNSS+ 2019*, pp. 465–484, 2019.

[16] B. DeCleene, "Defining Pseudorange Integrity - Overbounding," *International Technical Meeting of the Satellite Division of The Institute of Navigation (ION GPS 2000)*, no. September, pp. 1916 – 1924, 2000.

[17] J. Rife, S. Pullen, P. Enge, and B. Pervan, "Paired Overbounding for Nonideal LAAS and WAAS," *IEEE Transactions on Aerospace and Electronic Systems*, vol. 42, no. 4, pp. 1386–1395, 2006.

[18] Working Group C, "EU-U.S. Cooperation on Satellite Navigation Working Group C, ARAIM Technical Subgroup, Milestone 3 Report," tech. rep., 2016.

[19] S. E. Langel, *Bounding Estimation Integrity Risk for Linear Systems with Structured Stochastic Modeling Uncertainty*. PhD thesis, Illinois Institute of Technology, 2014.

[20] S. Langel, O. Garcia Crespillo, and M. Joerger, "Bounding Sequential Estimation Errors Due to Gauss-Markov Noise with Uncertain Time Constants," in *Proceedings of the ION GNSS+ 2019*, (Miami, Florida), September 2019.

[21] E. Gallon, M. Joerger, S. Perea, and B. Pervan, "Error Model Development for ARAIM Exploiting Satellite Motion," in *Proceedings of the ION GNSS+ 2019*, (Miami, Florida), September 2019.

[22] E. Gallon, M. Joerger, and B. Pervan, "Robust Modeling of Tropospheric Delay Dynamics for Sequential Positioning," in *IEEE/ION PLANS 2020*, (Portland, Oregon), 2020.

[23] L. Space Exploration Holdings, T. Hughes, and P. Cooper, "Application for Blanket Licensed Earth Stations," Tech. Rep. 2, 2019.

[24] M. Albulet and Space Exploration Technologies Corp., "SpaceX Non-Geostationary Satellite System - Attachment A," 2017.

[25] C. Henry, "SpaceX says more Starlink orbits will speed service, reduce launch needs." `https://spacenews.com/spacex-says-more-starlink-orbits-will-speed-service-reduce-launch-needs/`, 9 2019. (Accessed on 06/29/2020).

[26] M. Joerger, L. Gratton, B. Pervan, and C. E. Cohen, "Analysis of Iridium-augmented GPS for floating carrier phase positioning," *Navigation, Journal of the Institute of Navigation*, vol. 57, no. 2, pp. 137–160, 2010.

[27] J. Lee, Y. T. Morton, J. Lee, H. S. Moon, and J. Seo, "Monitoring and Mitigation of Ionospheric Anomalies for GNSS-Based Safety Critical Systems: A Review of Up-to-Date Signal Processing Techniques," *IEEE Signal Processing Magazine*, vol. 34, no. 5, pp. 96–110, 2017.

[28] M. Joerger, J. Neale, S. Datta-Barua, and B. Pervan, "Ionospheric Error Modeling for Carrier Phase-Based Multiconstellation Navigation Systems," *IEEE Transactions on Aerospace and Electronic Systems*, vol. 49, no. 1, pp. 451–467, 2013.

[29] T. Walter, J. Blanch, and P. Enge, "Evaluation of Signal in Space Error Bounds to Support Aviation Integrity," *NAVIGATION, Journal of the Institute of navigation)*, vol. 57, no. 2, pp. 101–113, Summer 2010.

[30] T. Walter and J. Blanch, "KEYNOTE - Characterization of GNSS Clock and Ephemeris Errors to Support ARAIM," in *Proceedings of the ION 2015 Pacific PNT Meeting*, (Honolulu, Hawaii), pp. 920–931, April 2015.

[31] T. Walter, K. Gunning, R. Eric Phelts, and J. Blanch, "Validation of the Unfaulted Error Bounds for ARAIM," *Navigation: Journal of The Institute of Navigation*, vol. 65, no. 1, pp. 117–133, 2018.

[32] E. Gallon, M. Joerger, and B. Pervan, "Frequency-Domain Modeling of Orbit and Clock Errors for Sequential Positioning," in *ION GNSS+ 2020*, (St. Louis, Missouri), 2020.

[33] Radio Technical Commission for Aeronautics (RTCA) Special Committee 159, "Minimum Operational Performance Standards for Global Positioning System/Wide Area Augmentation System Airborne Equipment," 2006.

[34] Radio Technical Commission for Aeronautics (RTCA) Special Committee 159, "Minimum Operational Performance Standards for Global Positioning System/Wide Area Augmentation System Airborne Equipment," 2009.

[35] S. Khanafseh, B. Kujur, M. Joerger, T. Walter, S. Pullen, J. Blanch, K. Doherty, L. Norman, L. de Groot, and B. Pervan, "GNSS Multipath Error Modeling for Automotive Applications," *Proceedings of the 31st International Technical Meeting of The Satellite Division of the Institute of Navigation (ION GNSS+ 2018)*, pp. 1573–1589, 2018.

[36] M. Joerger, *Carrier Phase GPS Augmentation Using Laser Scanners and Using Low Earth Orbiting Satellites*. PhD thesis, Illinois Institute of Technology, 2009.

[37] B. Pervan, S. Khanafseh, and J. Patel, "Test Statistic Auto- and Cross-correlation Effects on Monitor False Alert and Missed Detection Probabilities," in *Proceedings of the 2017 International Technical Meeting of The Institute of Navigation*, (Monterey, California), pp. 562–590, January 2017.

[38] J. Haase, M. Ge, H. Vedel, and E. Calais, "Accuracy and Variability of GPS Tropospheric Delay Measurements of Water Vapor in the Western Mediterranean," *Journal of Applied Meteorology)*, vol. 42, pp. 1547–1568, November 2003.

[39] Working Group C, "EU-U.S. Cooperation on Satellite Navigation, Working Group C, ARAIM Technical Subgroup, Interim Report," tech. rep., 2012.

[40] Working Group C, "EU-US Cooperation on Satellite Navigation Working Group C, ARAIM Technical Subgroup, Milestone 2 Report," tech. rep., 2015.

[41] M. Joerger, F. C. Chan, and B. Pervan, "Solution Separation Versus Residual-Based RAIM," *Navigation, Journal of the Institute of Navigation*, vol. 61, no. 4, pp. 273–291, 2014.

[42] J. Blanch, T. Walter, P. Enge, Y. Lee, B. Pervan, M. Rippl, and A. Spletter, "Advanced RAIM user algorithm description: Integrity support message processing, fault detection, exclusion, and protection level calculation," in *25th International Technical Meeting of the Satellite Division of the Institute of Navigation 2012, ION GNSS 2012*, vol. 4, pp. 2828–2849, 2012.

[43] P. B. Ober, "Ways to Improve RAIM/AAIM Availability Using Position Domain Performance Computations," *Proceedings of the National Technical Meeting, Institute of Navigation*, pp. 485–497, 1997.

[44] Y. Lee, "New Techniques Relating Fault Detection and Exclusion Performance to GPS Primary Means Integrity Requirements," *Proceedings of ION GPS*, vol. 2, pp. 1929–1939, 1995.

[45] C. Milner, B. Pervan, J. Blanch, and M. Joerger, "Evaluating Integrity and Continuity Over Time in Advanced RAIM," *2020 IEEE/ION Position, Location and Navigation Symposium, PLANS 2020*, pp. 502–514, 2020.

[46] U.S. Department of Defense, *Global Positioning System Standard Positioning Service Performance Standard (GPS SPS PS)*. 5 ed., April 2020.